

Perpendicularly Magnetized Thin-Film Antidot Arrays for Superparamagnetic Microbead Actuation

Minae Ouk^{1b} and Geoffrey S. D. Beach

Department of Materials Science and Engineering, Massachusetts Institute of Technology, Cambridge, MA 02139 USA

We report the directed transport of superparamagnetic microbeads (SPBs) on antidot arrays patterned from multilayered Co/Pt films with perpendicular magnetic anisotropy (PMA). The dynamics of water-suspended SPBs driven across the substrate surface by elliptical rotating magnetic fields is studied experimentally and modeled analytically. Bead motion on PMA substrates is shown to be significantly faster than on similarly patterned films based on in-plane magnetized materials. Furthermore, we show different SPB trajectories on different lattice geometries, suggesting that the magnetic potential distribution plays a crucial role in determining the dynamics. Our findings provide new insights into the enhanced transport of SPBs using PMA thin films as stray field sources that enable dynamic magnetic potential landscapes.

Index Terms—Magnetic devices, magnetic multilayers, magnetic particles, perpendicular magnetic anisotropy (PMA).

I. INTRODUCTION

THE transport of magnetic particles has widely been studied in colloidal systems for controlling and sorting biological entities in lab-on-a-chip devices [1]–[13]. Owing to the broad availability of micrometer- and nanometer-sized functionalized superparamagnetic microbeads (SPBs) and the rapid development of effective means to manipulate them, chip-based magnetic actuation is emerging as an extremely promising way to facilitate in-fluid handling of biological species in a variety of applications.

In recent decades, there have been many studies inducing bead motion based on magnetic systems, which have many advantages. Discrete permanent magnets or electromagnets can manipulate magnetic particles without interference with microfluidic or biological processes [14], [15]. Furthermore, magnetic systems do not need complex experimental components such as reservoir chambers, pumps for flow, microchannels, or electrical connections for sensing [6]. Magnetic fields do not degrade biological entities and their action is generally independent of the fluid matrix, and they do not generate heating that would destabilize sensitive biological entities [16], [17].

Several promising approaches have been studied to manipulate microbeads collectively and even individually using lithographically patterned thin-film magnetic microstructures [7] or ferromagnetic tracks [18]–[26]. Periodic patterned magnetic structures in which external fields generate dynamically tunable potential energy landscape have been of particular interest [27]–[31]. In such systems, a combination of a time-periodic (i.e., rotating) external magnetic drive field and a spatially periodic pattern of magnetic features with engineered local stray fields allow for the generation of translatable potential energy wells for superparamagnetic

particles. This can enable directed transport, as well as sorting operations by optimizing and utilizing magnetophoretic properties. To this end, the dynamics of microbead transport using micrometer-scale magnetic dots or antidots patterned into thin-film magnetic arrays has been studied in detail [32]. Bead transport is found to exhibit several dynamical regimes when driven by a rotating magnetic field, including a low-frequency regime in which beads hop from one point in the array to another on each field rotation cycle, and a high-frequency regime in which hydrodynamic drag leads to a more complex dynamics and a drop in the average translation velocity [31]. The critical frequency separating these regimes, and hence the maximum transport speed that can be achieved, depends on the strength of the magnetic driving force with respect to hydrodynamic drag. So far, the majority of studies have focused on in-plane magnetized thin films [32]–[35], where stray fields usually arise from closure domains that form at the edges [32], [36]–[38]. In such cases, the stray fields are less strong than could be achieved using single-domain entities with stray fields generated by free surface poles.

In this paper, we examine microbead transport using perpendicularly magnetized thin films in which stray fields in patterned antidot arrays facilitate strong magnetostatic interactions that allow ultrathin film-based structures to transport beads at high speed compared to in-plane magnetized structures. We study the transport dynamics and transport modes experimentally and use micromagnetic and numerical modeling to elucidate the transport processes in detail. We focus on multilayered Co/Pt films with interfacial perpendicular magnetic anisotropy (PMA) and examine the motion of fluid-suspended SPBs under the influence of a rotating elliptical magnetic field. In addition to strong stray fields, these structures exhibit a large coercivity (H_c), which directly corresponds to the maximum magnetic fields that can be applied to drive SPB motion without switching the magnetic state of the film [32], [39]–[42]. Two crucial parameters that relate to the dynamics, namely, the threshold fields and frequencies, are obtained for structures with several array symmetries. Interestingly, we find that the dynamics of SPBs are

Manuscript received September 12, 2018; revised February 17, 2019; accepted May 12, 2019. Date of publication June 12, 2019; date of current version August 19, 2019. Corresponding author: G. S. D. Beach (e-mail: gbeach@mit.edu).

Color versions of one or more of the figures in this paper are available online at <http://ieeexplore.ieee.org>.

Digital Object Identifier 10.1109/TMAG.2019.2918264

0018-9464 © 2019 IEEE. Personal use is permitted, but republication/redistribution requires IEEE permission. See http://www.ieee.org/publications_standards/publications/rights/index.html for more information.

enhanced and their working field ranges are wider using PMA films as compared to similar films exhibiting in-plane magnetic anisotropy (IMA) [39]. Based on analytical model calculations, we find that the magnetic potential distribution and force is the key to understanding the dynamics of SPBs. Our work suggests that PMA antidot patterns offer the possibility for improving the movement of SPBs as well as flexibility for the conditions in the bead motion.

II. MATERIALS AND EXPERIMENTAL METHODS

In this paper, we used a standard optical lithography and lift-off technique to create antidot array structures with different lattice symmetries on thermally oxidized Si(100) wafers as shown in Fig. 1 [38], [39], [43]. After resist patterning and development, thin films with the structure Ta(3 nm)/Pt(5 nm)/[Co(1 nm)/Pt(5 nm)]₅ were deposited using dc magnetron sputtering at room temperature at an Ar pressure of 3.0 mTorr. Following liftoff, the wafers were coated with a 80 nm thick protective SiO₂ layer by RF sputtering at room temperature at an Ar pressure of 3.0 mTorr. We fabricated both square and hexagonal lattices, with hole diameter of 2.9 μm and center-to-center spacing of 5.0 μm.

We used superparamagnetic beads with a mean diameter of 2.8 μm (DynabeadsM-270 Carboxylic Acid from ThermoFisher—catalog number 14305D), diluted in deionized water. Dilute bead suspensions were placed in a polydimethylsiloxane (PDMS) well on the substrate, and then sealed with a microscope cover slip. These samples were placed on a customized electromagnet that was composed of an out-of-plane field air coil and in-plane quadrupole magnet for applying the rotating field. The magnets can generate an in-plane field ($\mu_0 H_{IP}$) of up to ~50 mT and out-of-plane field ($\mu_0 H_{OOP}$) of up to ~40 mT. As shown schematically in Fig. 1(a), we applied rotating magnetic fields, defined as $H_{IP}(t) = H_{IP}\sin(2\pi ft)$ and $H_{OOP}(t) = H_{OOP}\cos(2\pi ft)$, with various field ellipticities (ratio of H_{IP} to H_{OOP}) in the xz plane to observe the movement of the SPBs.

SPB motion was monitored using a home-built microscope integrated into the custom electromagnet stage setup. The microscope included a CCD camera fitted to a long working distance microscope objective (Mitutoyo10x M Plan APO). Individual bead trajectories were extracted from video segments captured during rotating field application, with durations of at least 10 s captured at a frame rate of 70 frames per second. A custom software tracking tool was used to track individual beads within a 0.2×0.2 mm² imaged region. Mean individual bead velocities were computed as the ratio of the net linear displacement to the elapsed time. We note that some beads exhibit discontinuous motion due to adhesion that we ascribe to nonspecific binding from bead-substrate chemical interactions [44] due to its random occurrence and variability depending on substrate rinsing procedures. We exclude such beads from our velocity analysis and include only those that show continuous, uniform motion for at least 10 s. The average velocity v reported below is taken as the mean of the individual velocities of approximately 90–130 beads under each experimental condition, and the standard deviation is taken from the set of measured individual velocities.

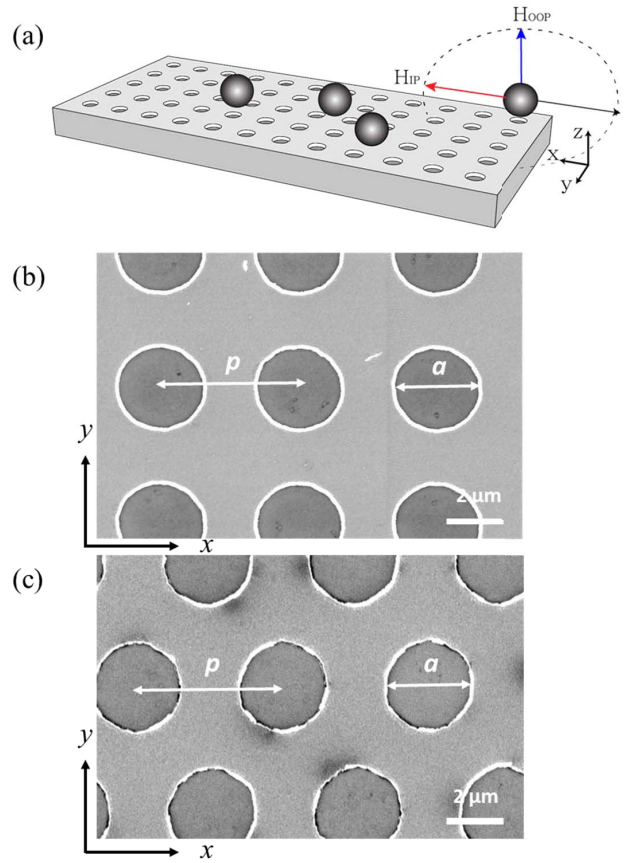


Fig. 1. (a) Schematic of the superparamagnetic bead motion experiments. The blue arrow represents the amplitude of the out-of-plane field H_{OOP} and the red arrow shows the amplitude of the in-plane field H_{IP} . (b), (c) Scanning electron micrograph images of Co/Pt antidot arrays with (b) square lattice and (c) hexagonal lattice symmetry. The periodicity of both patterns is 5.0 μm and the diameter of the holes is 2.9 μm for both lattices.

In order to further understand the experimental phenomena in more detail, we conducted micromagnetic simulations and calculated the profiles of stray fields and magnetostatic potential landscapes as a function of field rotation angle and amplitude. In the micromagnetic simulations, the system was divided into $4 \times 4 \times 40$ nm³ cells, a size that is slightly smaller than the exchange length of ~5 nm. The material parameters consistent with bulk Co were used: saturation magnetization $M_s = 1.4 \times 10^6$ Am⁻¹, exchange stiffness constant $A = 3 \times 10^{-11}$ Jm⁻¹, and a uniaxial out-of-plane anisotropy constant $K_u = 5 \times 10^3$ J/m³. To simplify the simulation process, we modeled the multilayer as a continuous film scaling the micromagnetic parameters using the usual effective medium approach [45], [46]. The magnetostatic potential energy of SPBs was approximated by integrating the dipolar energy density $-\mathbf{M} \cdot \mathbf{B}$ over the bead volume. In this step, we assumed the bead magnetization is given by $\mathbf{M} = \chi \mathbf{B}$ with the volume susceptibility χ taken as 800 kA·m⁻¹·T⁻¹, which is suitable for the commercial SPBs used in these experiments [8].

III. RESULTS AND DISCUSSION

Fig. 1(b) and (c) shows scanning electron micrographs of the Co/Pt antidot arrays with periodicity $p = 5$ μm and hole

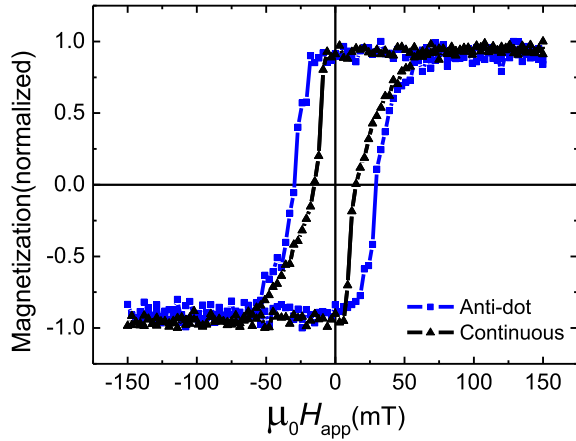


Fig. 2. Out-of-plane hysteresis loop of unpatterned (continuous) and patterned (anti-dot) Co/Pt multilayer film with hexagonal lattice symmetry.

diameter of $2.9 \mu\text{m}$ with square and hexagonal lattice symmetry, respectively. Fig. 2 shows the out-of-plane hysteresis loops measured using a vibrating sample magnetometer for an unpatterned reference film and a patterned film. The results show square loops with full out-of-plane remanence in both cases, confirming PMA with a single-domain remanent state. The coercivity $\mu_0 H_c$ of the patterned sample is $\sim 30 \text{ mT}$, which is slightly larger than in the unpatterned continuous film as seen elsewhere [39]. The larger H_c is an important factor in the dynamics of bead movement, and it is expected to make possible a wider working field range for SPB motion.

Fig. 3 shows the average velocity v of SPBs and standard deviation (plotted as an error bar) as a function of f for bead motion on a film patterned with square symmetry and hexagonal symmetry. Here, the field rotation plane is in the xz plane (Fig. 1). The field rotation frequency f is varied from 0 to 25 Hz at $\mu_0 H_{\text{OOP}} = 4 \text{ mT}$ and $\mu_0 H_{\text{IP}} = 3 \text{ mT}$. The v as a function of f exhibits a similar behavior as reported by Yellen *et al.* [31] in periodically patterned substrates in which up to the critical frequency f_c , the velocity linearly increases and beyond the critical frequency the average velocity rapidly falls off. In Fig. 3, the f_c is approximately 4.0 and 4.5 Hz for the square lattice and the hexagonal lattice, respectively. Although the high f_c leads to a high maximum v , the maximum v of the square lattice is 1.5 times higher than that of the hexagonal lattice. It is surprising that the v of the square lattice is generally higher than for the hexagonal lattice even if the patterns have the same hole diameter and periodicity. We will analyze this phenomenon based on the micromagnetic simulations and the trajectory of SPBs motion in Fig. 4.

We also show for reference the velocity–frequency curve using a square-lattice array with similar dimensions based on an in-plane magnetized 40 nm-thick Co film [32]. We see that the critical velocity of SPBs on the PMA film is around $20 \mu\text{m/s}$, which is significantly higher than the $15 \mu\text{m/s}$ critical velocity observed for the in-plane case, despite the fact that the total volume of ferromagnetic material is eight times smaller. However, stronger stray field interactions are nonetheless achieved owing to the high stray fields from the free pole distribution in the PMA case.

Next, we analyzed the relationship between v and f using a standard magnetophoretic transport model [27], [29], [31]. The basic concept of the model is that on the periodic dot arrays, the magnetization in the SPBs periodically rotates following the rotation of the applied field, while the stray field profile of the underlying magnetic pattern remains the same. The mutual stray field interactions then give rise to a potential minimum whose position translates continuously. The gradient of this minimum yields a force that drags the bead up to a velocity limit where the hydrodynamic drag balances the maximum magnetic force achievable by the periodic potential. Beyond this critical velocity, the bead cannot keep up with the rotating field and tends to exhibit an oscillatory behavior with a smaller net displacement per unit time. The v – f curve can be described in this model by [31]

$$v = \begin{cases} \omega \frac{p}{2\pi} & \text{for } \omega \leq \omega_c \\ \left(\omega - \sqrt{\omega^2 - \omega_c^2} \right) \frac{p}{2\pi} & \text{for } \omega > \omega_c \end{cases} \quad (1)$$

where p is the center-to-center distance between adjacent energy minima, and $\omega_c = 2\pi f_c$ is related to the ratio of magnetic force to viscous drag. As seen in Fig. 3, this model fits the experimental data very well for the square lattice, in which motion is expected to be linear for field rotation plane parallel to the lattice directions. However, the model fits the data for the hexagonal lattice less well. Notably, (1) cannot describe the observed data when the linear distance for field revolution d is fixed equal to the center-to-center distance between adjacent holes in the hexagonal lattice along the x -direction [see Fig. 1(c)]. Instead, the data are better fitted by adjusting d to a value of $2.9 \mu\text{m}$, which is significantly less than the spacing between holes along the x -axis.

In order to understand the detailed motion on lattices with different symmetry and hence understand discrepancies with the above model, we have imaged the motion of SPBs from one lattice symmetry point to another (Fig. 4). Fig. 4(a) and (b) shows five steps of the SPB movement when the SPBs are traveling nominally along the x -direction. The SPB transport is observed as a hopping motion along the antidot array and they slightly move along the y -direction during the motion. The most notable difference between the SPB motion on the two lattices is that the trajectories follow a zig-zag shape on the hexagonal lattice, represented as the path A–B–A' in Fig. 4(b). Due to the zig-zag motion, the total traveling time on the hexagonal lattice is 1.4 s from A to A', while, for the same distance, it is 0.8 s on the square lattice. v of the SPBs on the hexagonal lattice decreases by 40% as compared to the square lattice with a more linear trajectory, which can be understood from the different local paths that the beads take. Since (1) assumes a linear trajectory, accounting for the net linear displacement due to the zig-zag path accounts for the discrepancy in the fitting in Fig. 3(b).

Next, we examined the effect of applied fields on the SPB motion. One might anticipate two field thresholds that could be important in ensuring bead motion: a lower threshold, which ensures sufficient magnetization of the SPBs to allow for potential energy well depths that are capable of supporting

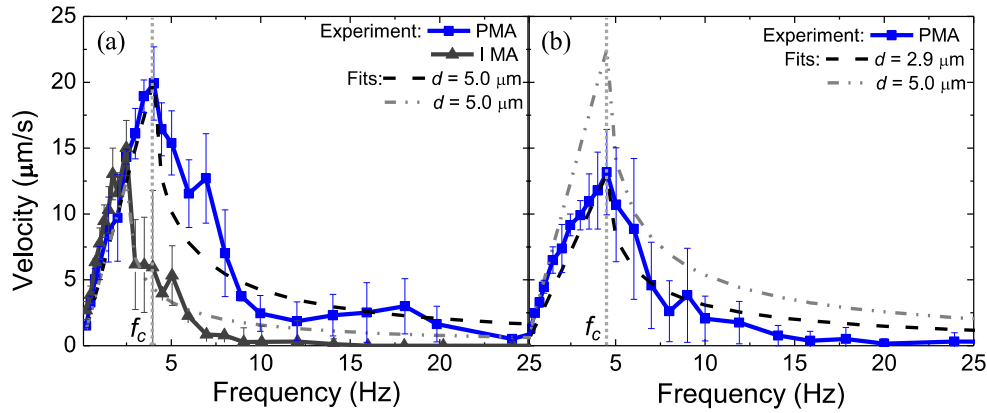


Fig. 3. Velocity as a function of frequency for $\mu_0 H_{OOP} = 4$ mT and $\mu_0 H_{IP} = 3$ mT on (a) square lattice and (b) hexagonal lattice. The solid lines and symbols are the experimental data for PMA and IMA films, and dashed lines are the analytical model calculations, with the critical frequency as the sole fitting parameter. The parameter d corresponds to the linear distance per period of field rotation used in the model. Data points for the IMA case correspond to are reproduced from [36, Fig. 2(b)] for the case of a 40 nm-thick Co film patterned as a square antidot array with similar dimensions as the square array used here.

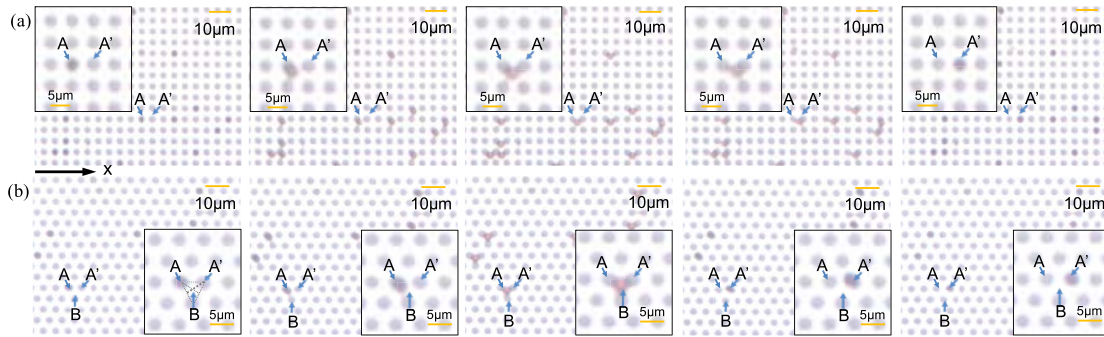


Fig. 4. Optical microscopy images showing a series of SPB movement snapshots taken (a) every 0.20 s on square lattice and (b) every 0.35 s on hexagonal lattice when the field ($\mu_0 H_{IP} = 3$ mT and $\mu_0 H_{OOP} = 4$ mT) is rotating clockwise at 1 Hz.

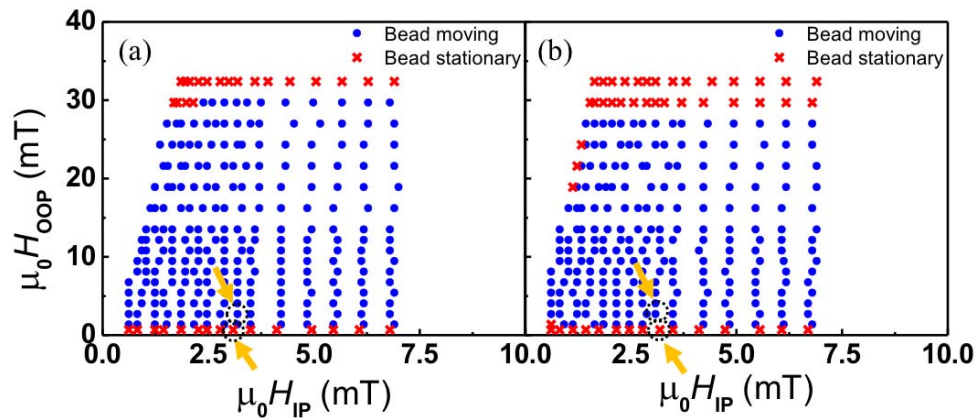


Fig. 5. Critical threshold of both H_{IP} and H_{OOP} for both observing bead motion at $f = 1$ Hz for (a) square lattice and (b) hexagonal lattice. The blue dot means that we can observe SPB translation and the red cross indicates that SPBs oscillate back and forth with zero net velocity.

transport; and an upper threshold set by the out-of-plane coercivity, beyond which both the bead magnetization and the film magnetization would reverse on each half-field cycle, which would preclude translation of a potential well from one magnetic hole to the next. Fig. 5(a) and (b) maps out the field parameter space in which bead motion is observed, using a rotating field frequency of 1 Hz, which is below f_c , and

varying the in-plane and out-of-plane field components. A blue dot indicates that most of the SPBs could be transported in each magnetic field combination, whereas a red cross indicates that SPB motions do not move, except for locally back-and-forth oscillations. We find that the transport of the SPBs occurs even at very small applied magnetic field, which would be beneficial for low-power operation, and the range between

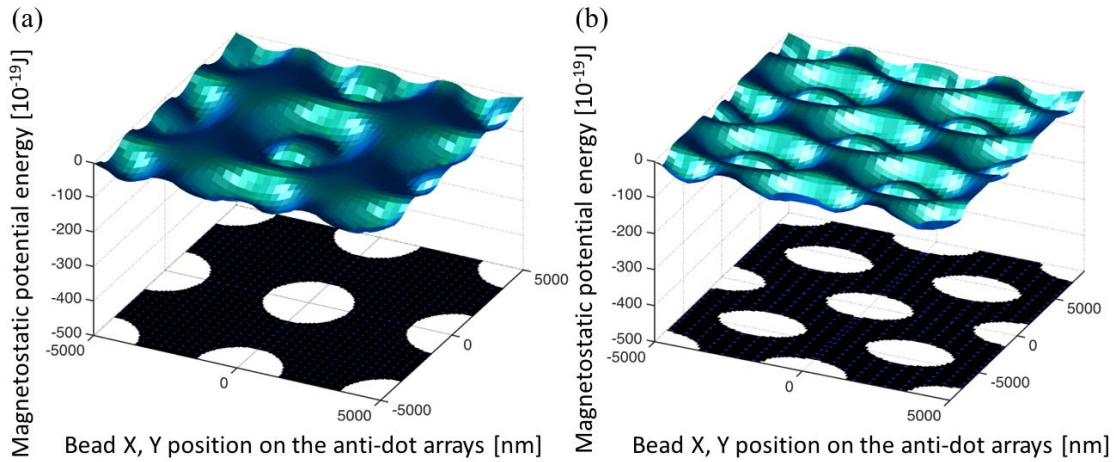


Fig. 6. Magnetostatic potential energy landscape at zero applied field for (a) square lattice symmetry and (b) hexagonal lattice symmetry.

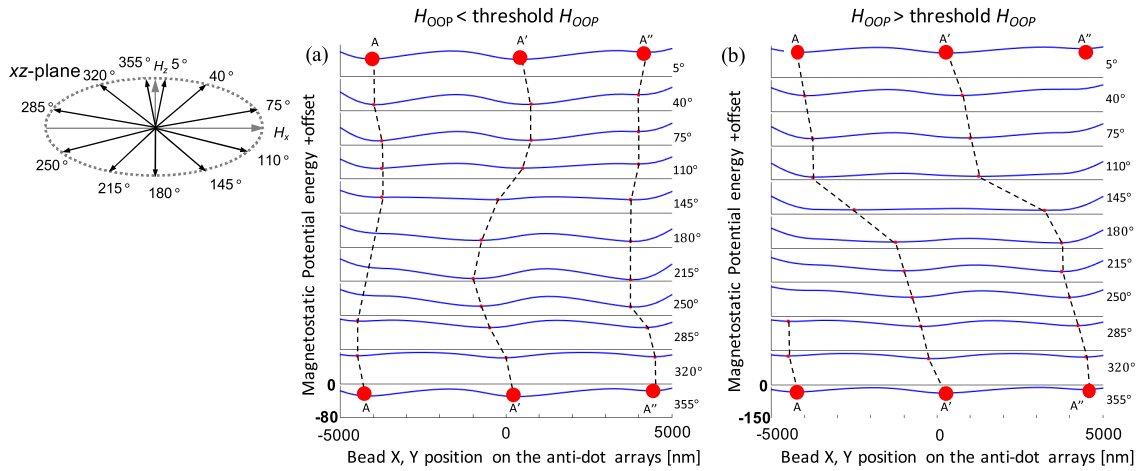


Fig. 7. Cross sections of potential energy landscape along the x -direction for the square lattice, computed as in Fig. 6 but with applied fields oriented at various angles θ in the field rotation plane (xz plane). (a) Case when the applied out-of-plane field is below the threshold for bead translation. (b) Case when the applied out-of-plane field is above the threshold for bead translation. The red dotted lines follow the local potential energy minima, during one field rotation cycle, in the cases that the out-of-plane field is below the threshold for translation, and above that threshold.

minimum and maximum out-of-plane field is quite large. The operating field range is much larger than that found for similar patterned films based on in-plane magnetized materials with weaker anisotropy and stray field interactions [39].

Finally, we describe analytical calculations of the potential landscape (SPB energy as a function of position, under various applied field conditions), based on the stray field profiles of the micromagnetically simulated magnetization profiles. Owing to the strong PMA, the magnetization is uniform in the case of zero applied fields and deviates only slightly from this state under the action of modest rotating applied fields. Fig. 6(a) and (b) shows the energy surfaces for 2.8 μm SPBs on the square antidot array and on the hexagonal antidot array, respectively, without applying a magnetic field. The depths of the potentials well are quantitatively similar to each other, and the minimum positions are observed around the rims of the holes for both lattices. Similar potential landscapes were computed as a function of applied magnetic field angle for an elliptical field with $\mu_0 H_{IP} = 3.09$ mT and $\mu_0 H_{OOP} = 0.675$ mT [Fig. 7(a)] and for $\mu_0 H_{IP} =$

3.19 mT and $\mu_0 H_{OOP} = 2.7$ mT [Fig. 7(b)], for one full rotation of the field vector. These fields correspond to the experimental points marked by yellow arrows in Fig. 5(a), on either side of the experimental critical lower field threshold for bead motion. Cross sections for the potential landscape along the x -direction, passing through the potential minima, are shown in Fig. 7(a) and (b) for various field rotation angles. Dotted lines follow continuous translation of the local potential minima, which represent the expected trajectories of the SPBs during field rotation. One sees that in the low-field case, the SPBs move back to the same position (A to A) and locally oscillate back and forth after a 360° rotation of the magnetic field. This phenomenon is different from that in Fig. 7(b), in which the positions of the minima continuously propagate to the right. In Fig. 7(b), the SPBs can be transported from A to A', while the magnetic field rotates a 360°. Therefore, these results clearly explain two different types of SPB movement: oscillation below the threshold field and transport above the threshold field. In addition, the depth of the magnetostatic potential well in Fig. 7(a) is shallower than that of Fig. 7(b).

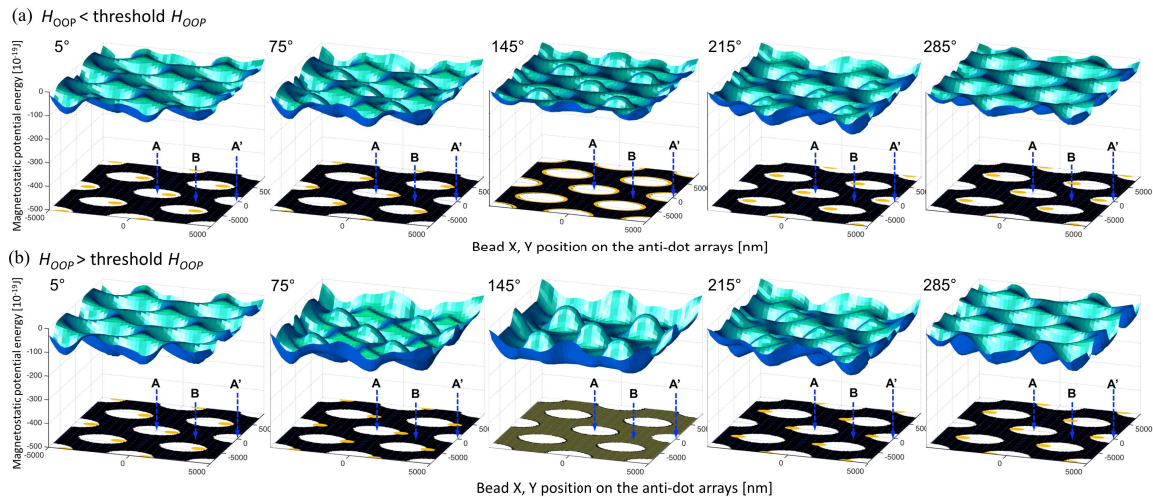


Fig. 8. Relaxed magnetization configuration and magnetostatic potential well of the hexagonal lattice for every 70° (a) below the threshold value and (b) above the threshold value in Fig. 5(b).

Thus, the magnetic force at Fig. 7(a) is smaller, and it is not sufficient to support SPB transport. Following the discussion above, these results show the origins of minimum thresholds in the magnetic fields on the square antidot array.

Finally, to understand the zig-zag motion on the hexagonal lattice, we also calculated the magnetic potential energy of the hexagonal lattice for $2.8 \mu\text{m}$ bead at two different magnetic field combinations: 1) below the threshold field and 2) above the threshold field. Fig. 8 describes the sequential potential energy landscapes at the same angle intervals for a rotation of the applied field. The yellow indicates the minimum positions of potential energy landscapes. Comparing the upper row to the lower row, the minimum positions have different behaviors when changing the angle of the rotating field. Fig. 8(a) describes the oscillation behavior of the SPBs, where the minimum positions slowly move to the right, but move back to the left after 145° . At around 145° , the SPBs can be located around the rim of the hole, where the depths of minimum positions are the same from one hole to the next. On the other hand, Fig. 8(b) describes the zig-zag motion (A–B–A') of the SPB transport in Fig. 4(b). As the field rotates, the energy minima continuously proceed to the right. At around 145° , where the minimum position can be located everywhere except for the inside of the hole, the SPBs can be located, and freely move between the holes including B areas. Therefore, the SPBs can be transported to the right, which is different from the lower field case. These simulations together with the ones presented in Fig. 5(b) describe the origin for the threshold in the magnetic field and explain the origin of SPB movement in zig-zag shape in Fig. 4(b).

IV. CONCLUSION

Using ordered antidot arrays with PMA, the SPBs can be effectively manipulated and transported, subject to thresholds in rotating field amplitude and frequency. Bead motion is found to be faster on PMA-based arrays as compared to those with in plane magnetization, which is attributed to the stronger stray field in the former. This allows for much thinner films to

be used, while still supporting stronger stray field interactions and hence enabling faster transport.

ACKNOWLEDGMENTS

The authors would like to thank A. Alexander-Katz and K. Gadelrab for computational support. M. Ouk acknowledges support from the Kwanjeong Educational Foundation.

REFERENCES

- [1] B. B. Yellen, D. S. Halverson, and G. Friedman, "Arranging matter by magnetic nanoparticle assembly," in *Proc. IEEE Int. Magn. Conf. (INTERMAG)*, Jan. 2006, p. 246.
- [2] G. Vieira *et al.*, "Magnetic wire traps and programmable manipulation of biological cells," *Phys. Rev. Lett.*, vol. 103, no. 12, 2009, Art. no. 128101.
- [3] G. Ruan *et al.*, "Simultaneous magnetic manipulation and fluorescent tracking of multiple individual hybrid nanostructures," *Nano Lett.*, vol. 10, no. 6, pp. 2220–2224, 2010.
- [4] Q. Ramadan, C. Yu, V. Samper, and D. P. Poenar, "Microcoils for transport of magnetic beads," *Appl. Phys. Lett.*, vol. 88, no. 3, 2006, Art. no. 032501.
- [5] C. S. Lee, H. Lee, and R. M. Westervelt, "Microelectromagnets for the control of magnetic nanoparticles," *Appl. Phys. Lett.*, vol. 79, pp. 3308–3310, Nov. 2001.
- [6] L. Johansson *et al.*, "A magnetic microchip for controlled transport of atomole levels of proteins," *Lab Chip*, vol. 10, no. 5, pp. 654–661, 2010.
- [7] K. Gunnarsson *et al.*, "Programmable motion and separation of single magnetic particles on patterned magnetic surfaces," *Adv. Mater.*, vol. 17, pp. 1730–1734, Jul. 2005.
- [8] R. J. S. Derks, A. Dietzel, R. Wimberger-Friedl, and M. W. J. Prins, "Magnetic bead manipulation in a sub-microliter fluid volume applicable for biosensing," *Microfluidics Nanofluidics*, vol. 3, no. 2, pp. 141–149, 2007.
- [9] J. D. Adams, U. Kim, and H. T. Soh, "Multitarget magnetic activated cell sorter," *Proc. Nat. Acad. Sci. USA*, vol. 105, pp. 18165–18170, Nov. 2008.
- [10] N. Pamme and A. Manz, "On-chip free-flow magnetophoresis: Continuous flow separation of magnetic particles and agglomerates," *Anal. Chem.*, vol. 76, pp. 7250–7256, Dec. 2004.
- [11] T. Lund-Olesen, H. Bruus, and M. F. Hansen, "Quantitative characterization of magnetic separators: Comparison of systems with and without integrated microfluidic mixers," *Biomed. Microdevices*, vol. 9, pp. 195–205, Apr. 2007.
- [12] J. Loehr, M. Loenne, A. Ernst, D. de las Heras, and T. M. Fischer, "Topological protection of multiparticle dissipative transport," *Nature Commun.*, vol. 7, Jun. 2016, Art. no. 11745.

- [13] L. E. Helseth, T. M. Fischer, and T. H. Johansen, "Magnetic structuring and transport of colloids at interfaces," *J. Magn. Magn. Mater.*, vol. 277, no. 3, pp. 245–250, 2004.
- [14] I. Šafařík and M. Šafaříková, "Use of magnetic techniques for the isolation of cells," *J. Chromatogr. B, Biomed. Sci. Appl.*, vol. 722, pp. 33–53, Feb. 1999.
- [15] M. A. M. Gijs, "Magnetic bead handling on-chip: New opportunities for analytical applications," *Microfluidics Nanofluidics*, vol. 1, pp. 22–40, Nov. 2004.
- [16] Q. A. Pankhurst, J. Connolly, S. K. Jones, and J. Dobson, "Applications of magnetic nanoparticles in biomedicine," *J. Phys. D, Appl. Phys.*, vol. 36, p. R167, Jun. 2003.
- [17] W. M. Arnold, "Positioning and levitation media for the separation of biological cells," *IEEE Trans. Ind. Appl.*, vol. 37, no. 5, pp. 1468–1475, Sep. 2001.
- [18] M. T. Bryan *et al.*, "Switchable cell trapping using superparamagnetic beads," *IEEE Magn. Lett.*, vol. 1, 2010, Art. no. 1500104.
- [19] M. T. Bryan, J. Dean, T. Schreffl, F. E. Thompson, J. Haycock, and D. A. Allwood, "The effect of trapping superparamagnetic beads on domain wall motion," *Appl. Phys. Lett.*, vol. 96, no. 19, 2010, Art. no. 192503.
- [20] E. Rapoport and G. S. D. Beach, "Dynamics of superparamagnetic microbead transport along magnetic nanotracks by magnetic domain walls," *Appl. Phys. Lett.*, vol. 100, no. 8, 2012, Art. no. 082401.
- [21] S. Anandakumar, V. S. Rani, S. Oh, B. L. Sinha, M. Takahashi, and C. Kim, "Translocation of bio-functionalized magnetic beads using smart magnetophoresis," *Biosensors Bioelectron.*, vol. 26, pp. 1755–1758, Dec. 2010.
- [22] E. Rapoport, D. Montana, and G. S. D. Beach, "Integrated capture, transport, and magneto-mechanical resonant sensing of superparamagnetic microbeads using magnetic domain walls," *Lab Chip*, vol. 12, no. 21, pp. 4433–4440, 2012.
- [23] M. Donolato *et al.*, "On-chip manipulation of protein-coated magnetic beads via domain-wall conduits," *Adv. Mater.*, vol. 22, pp. 2706–2710, Jun. 2010.
- [24] M. Donolato *et al.*, "Magnetic domain wall conduits for single cell applications," *Lab Chip*, vol. 11, no. 17, pp. 2976–2983, 2011.
- [25] M. Donolato, F. Lofink, S. Hankemeier, J. M. Porro, H. P. Oepen, and P. Vavassori, "Characterization of domain wall-based traps for magnetic beads separation," *J. Appl. Phys.*, vol. 111, no. 7, 2012, Art. no. 07B336.
- [26] A. Sarella, A. Torti, M. Donolato, M. Pancaldi, and P. Vavassori, "Two-dimensional programmable manipulation of magnetic nanoparticles on-chip," *Adv. Mater.*, vol. 26, no. 15, pp. 2384–2390, 2014.
- [27] B. B. Yellen and L. N. Virgin, "Nonlinear dynamics of superparamagnetic beads in a traveling magnetic-field wave," *Phys. Rev. E, Stat. Phys. Plasmas Fluids Relat. Interdiscip. Top.*, vol. 80, no. 1, 2009, Art. no. 011402.
- [28] A. D. Henriksen, N. Rozlosnik, and M. F. Hansen, "Geometrical optimization of microstripe arrays for microbead magnetophoresis," *Biomicrofluidics*, vol. 9, no. 5, 2015, Art. no. 054123.
- [29] L. Gao, M. A. Tahir, L. N. Virgin, and B. B. Yellen, "Multiplexing superparamagnetic beads driven by multi-frequency ratchets," *Lab Chip*, vol. 11, no. 24, pp. 4214–4220, 2011.
- [30] M. A. Tahir, L. Gao, L. N. Virgin, and B. B. Yellen, "Transport of superparamagnetic beads through a two-dimensional potential energy landscape," *Phys. Rev. E, Stat. Phys. Plasmas Fluids Relat. Interdiscip. Top.*, vol. 84, no. 1, 2011, Art. no. 011403.
- [31] B. B. Yellen, R. M. Erb, H. S. Son, R. Hewlin, Jr., H. Shang, and G. U. Lee, "Traveling wave magnetophoresis for high resolution chip based separations," *Lab Chip*, vol. 7, no. 12, pp. 1681–1688, 2007.
- [32] M. Ouk and G. S. D. Beach, "Superparamagnetic microbead transport induced by a magnetic field on large-area magnetic antidot arrays," *J. Magn. Magn. Mater.*, vol. 444, pp. 218–226, Dec. 2017.
- [33] N. G. Deshpande *et al.*, "Tailoring of magnetic properties of patterned cobalt antidots by simple manipulation of lattice symmetry," *Appl. Phys. Lett.*, vol. 96, no. 12, 2010, Art. no. 122503.
- [34] S. Tacchi *et al.*, "Angular dependence of magnetic normal modes in NiFe antidot lattices with different lattice symmetry," *IEEE Trans. Magn.*, vol. 46, no. 6, pp. 1440–1443, Jun. 2010.
- [35] P. Vavassori *et al.*, "Lattice symmetry and magnetization reversal in micron-size antidot arrays in permalloy film," *J. Appl. Phys.*, vol. 91, no. 10, pp. 7992–7994, 2002.
- [36] A. Manzin and O. Bottauscio, "Micromagnetic modelling of the anisotropy properties of permalloy antidot arrays with hexagonal symmetry," *J. Phys. D, Appl. Phys.*, vol. 45, no. 9, 2012, Art. no. 095001.
- [37] P. Warnicke, S. Felton, K. Gunnarsson, and P. Svedlindh, "Simulations of magnetic microstructure in thin film elements used for programmable motion of magnetic particles," *J. Magn. Magn. Mater.*, vol. 303, pp. 294–298, Aug. 2006.
- [38] C. C. Wang, A. O. Adeyeye, and N. Singh, "Magnetic antidot nanostructures: Effect of lattice geometry," *Nanotechnology*, vol. 17, no. 6, p. 1629, 2006.
- [39] S. N. Piramanayagam, M. Ranjbar, H. K. Tan, W. C. A. Poh, R. Sbiaa, and T. C. Chong, "Magnetic properties of antiferromagnetically coupled antidots of Co/Pd multilayers," *J. Appl. Phys.*, vol. 111, no. 7, 2012, Art. no. 07B916.
- [40] S. Pal *et al.*, "Optically induced spin wave dynamics in [Co/Pd]₈ antidot lattices with perpendicular magnetic anisotropy," *Appl. Phys. Lett.*, vol. 105, no. 16, 2014, Art. no. 162408.
- [41] M. T. Rahman, N. N. Shams, C. H. Lai, J. Fidler, and D. Suess, "Co/Pt perpendicular antidot arrays with engineered feature size and magnetic properties fabricated on anodic aluminum oxide templates," *Phys. Rev. B, Condens. Matter*, vol. 81, no. 1, 2010, Art. no. 014418.
- [42] D. Tripathy and A. O. Adeyeye, "Perpendicular anisotropy and out-of-plane exchange bias in nanoscale antidot arrays," *New J. Phys.*, vol. 13, no. 2, 2011, Art. no. 023035.
- [43] L. J. Heyderman, F. Nolting, D. Backes, and S. Czekaj, "Magnetization reversal in cobalt antidot arrays," *Phys. Rev. B, Condens. Matter*, vol. 73, no. 21, 2006, Art. no. 214429.
- [44] O. Florescu *et al.*, "On-chip magnetic separation of superparamagnetic beads for integrated molecular analysis," *J. Appl. Phys.*, vol. 107, Mar. 2010, Art. no. 054702.
- [45] A. Suna, "Perpendicular magnetic ground state of a multilayer film," *J. Appl. Phys.*, vol. 59, no. 2, pp. 313–316, 1986.
- [46] I. Lemesch, F. Büttner, and G. S. D. Beach, "Accurate model of the stripe domain phase of perpendicularly magnetized multilayers," *Phys. Rev. B, Condens. Matter*, vol. 95, no. 17, 2017, Art. no. 174423.